



HAL
open science

Turning Instrument Background Into Science Data for Structural Features of Radiation Belts

N. Yu. Ganushkina, Iannis Dandouras, M. W. Liemohn, H. Rème, J. Cao

► **To cite this version:**

N. Yu. Ganushkina, Iannis Dandouras, M. W. Liemohn, H. Rème, J. Cao. Turning Instrument Background Into Science Data for Structural Features of Radiation Belts. *Journal of Geophysical Research Space Physics*, 2021, 126, 10.1029/2021JA030014 . insu-03672335

HAL Id: insu-03672335

<https://insu.hal.science/insu-03672335>

Submitted on 19 May 2022

HAL is a multi-disciplinary open access archive for the deposit and dissemination of scientific research documents, whether they are published or not. The documents may come from teaching and research institutions in France or abroad, or from public or private research centers.

L'archive ouverte pluridisciplinaire **HAL**, est destinée au dépôt et à la diffusion de documents scientifiques de niveau recherche, publiés ou non, émanant des établissements d'enseignement et de recherche français ou étrangers, des laboratoires publics ou privés.



Distributed under a Creative Commons Attribution - NonCommercial - ShareAlike 4.0 International License

JGR Space Physics



TECHNICAL REPORTS: METHODS

10.1029/2021JA030014

Special Section:

Cluster 20th anniversary: results from the first 3D mission

Key Points:

- Instrument background counts reflect radiation belt features including temporal phenomena such as the storage ring
- Telemetry counts register signals which increase due to penetrating particles and can be used for radiation belt boundaries
- Data with indirect effects from energetic particles become of high value when no particle measurements are available

Correspondence to:

N. Y. Ganushkina,
ganuna@umich.edu

Citation:

Ganushkina, N. Y., Dandouras, I., Liemohn, M. W., Rème, H., & Cao, J. (2021). Turning instrument background into science data for structural features of radiation belts. *Journal of Geophysical Research: Space Physics*, 126, e2021JA030014. <https://doi.org/10.1029/2021JA030014>

Received 4 OCT 2021
Accepted 23 NOV 2021

© 2021. The Authors.

This is an open access article under the terms of the [Creative Commons Attribution-NonCommercial-NoDerivs](https://creativecommons.org/licenses/by-nc-nd/4.0/) License, which permits use and distribution in any medium, provided the original work is properly cited, the use is non-commercial and no modifications or adaptations are made.

Turning Instrument Background Into Science Data for Structural Features of Radiation Belts

N. Yu. Ganushkina^{1,2} , I. Dandouras³ , M. W. Liemohn² , H. Rème³ , and J. Cao⁴ 

¹Finnish Meteorological Institute, Helsinki, Finland, ²University of Michigan, Ann Arbor, MI, USA, ³Institut de Recherche en Astrophysique et Planétologie, Université de Toulouse/CNRS/UPS/CNES, Toulouse, France, ⁴School of Astronautics, Beijing University of Aeronautics and Astronautics, Beijing, China

Abstract Approaches regarding how to turn the instrument background counts into scientifically valuable data are presented in this Technical Report on Methods. The background counts due to penetrating energetic particles of radiation belts detected on Cluster CIS HIA and CODIF instruments and the Double Star HIA instrument are used in these approaches. In HIA spectrograms, the background counts are seen simultaneously in all energy channels marking the entry and exit of the radiation belts by the spacecraft, therefore, the locations of the boundaries of the outer and inner belts can be determined. In the case when HIA measurements are not readily available, a new method is proposed in which supplementary data streams within the CODIF telemetry is exploited. It employs separate counts that register “start,” “stop,” and “non-valid” signals increasing in the presence of penetrating particles even when no corresponding increase are shown in the energy-time spectrograms. The locations of the radiation belt boundaries are defined by following the changes in counts gradients with time and visual inspection of all the available measurements. The July–August 2007 and September–October 2012 time periods are analyzed for method demonstration on a presence of a third radiation belt, or storage ring.

1. Introduction

Earth's radiation belts have been the observational target on numerous satellites starting from Explorer 1 and 3 and Sputnik 2 and 3 to the most recent missions, the Van Allen Probes (called earlier Radiation Belt Storm Probes [RBSP]) twin spacecraft and the Japanese Exploration of energization and Radiation in Geospace “Arase” (ERG) probe. The direct measurements of energetic particles and other quantities of radiation belts provide the most information on the complexity of the radiation belts dynamics. In case when no mission is operating and no direct observations of radiation belts are available, other types of measurements become of critical importance. Data containing indirect effects from the energetic particles in the radiation belts detected as background counts by the instruments not designed to measure radiation belts particles can be the only source for further development and validation of the radiation belts' models.

Using the advantage of changes in Cluster orbit in 2007–2009 which brought it very close to the Earth (perigee at around $L = 2$, where L is the McIlwain parameter) and availability of the Double Star data, Ganushkina et al. (2011) provided the direct evidence that the background counts in HIA (Hot Ion Analyzer) and CODIF (COMposition and DIstribution Function) instruments due to penetration of energetic particles of radiation belts can determine the locations of the boundaries of the outer and inner belts. The assumption that the measured background is due to >2 MeV (megaelectronvolt) electrons was proven by the simulations using the Casino (Monte Carlo Simulation of Electron Trajectory in Solids, <http://www.gel.usherbrooke.ca/casino/>). At the same time, this 2 MeV threshold is not an absolute one, since the contamination can also come from the gamma-rays emitted by incoming electrons via the Bremsstrahlung process (e.g., Kasahara et al., 2009). For the proton background, 30 MeV as the low threshold energy was proved using the SRIM (The Stopping and Range of Ions in Matter, <http://www.srim.org/>) simulation software. Keeping in mind the above mentioned assumptions, it was nevertheless possible to study the variations of the determined radiation belt boundaries with time and solar wind driving and draw conclusions on the slot region widening due to weaker inward radial diffusion and weak local acceleration.

Background counts can define specific features in the radiation belt fluxes as, for example, the discovery of a storage ring (Baker et al., 2013) following the launch of the Van Allen Probes. This transient feature was observed

as a ring of energetic (>2 MeV) electrons located between L-shells of 3 and 3.5 separate from the traditional radiation belts. This additional belt was formed on September 2, 2012 following the arrival of an interplanetary shock, it was present for about four weeks and it disappeared on October 1, 2012.

In later studies, storage ring feature was also called a third belt and, more recently, a remnant belt as more understanding of the nature of it has appeared. Turner et al. (2013) analyzed THEMIS (Time History of Events and Macroscale Interactions during Substorms) SST (Solid State Telescope) data and reported 13 events when two peaks were observed in the electron phase space density (with energies from ~ 400 keV to several MeV) in the outer radiation belt region. Yuan and Zong (2013) found eight events when the radiation belts exhibited three belts using data from the low-altitude SAMPEX (Solar Anomalous and Magnetospheric Particle Explorer) spacecraft. Kellerman et al. (2014) reanalyzed the available data during the March 1991 storm and found clear presence of a storage ring. As more Van Allen Probes data became available, Baker et al. (2016) reported the signatures of storage ring during two storms in 2015 and later Pinto et al. (2018) identified 30 three-belt events between September 2012 and November 2017 with energy peaked at 5.2 MeV and the lifetime ranged from days at 1.8 MeV up to months at 6.3 MeV. The most recent study by Hao et al. (2020) found double peaks at $L = 3.5$ and $L = 4.5$ in 500–800 keV electron spectrograms present for 2–3 days during September 2017 storm. Baker et al. (2013) suggested that the appearance of the storage ring was related to the loss of the electrons in the outer radiation belt, but not to the freshly injected particles. The formation of such three-belt structure was attributed by Mann et al. (2013) to radial transport of electrons driven by ULF (ultra-low frequency) waves. Later simulation studies by Shprits et al. (2013); Shprits et al. (2018) demonstrated the role of scattering by electromagnetic ion cyclotron waves to the Earth's atmosphere. They showed that the storage ring electrons can remain trapped for a long time due to the absence of resonant interactions with very-low-frequency plasma waves at low latitudes and, as a consequence, no scattering. Pinto et al. (2019) using Van Allen Probes measurements inside the plasmasphere found a good agreement between the observed decay rates with theoretical lifetimes of ultra-relativistic electrons for losses due to hiss waves based on recent statistics of hiss waves and plasmaspheric density.

In the present paper, we will use the original name “storage ring” as was given in Baker et al. (2013). This particular noticeable feature is used here to demonstrate based on Cluster data the strength of the method to determine the finer specifics and temporal features in the radiation belts from the measured background, not only the usually well-observed locations of the outer and inner belts. This method is rather straightforward and applicable when the data from electrostatic analyzer instrument HIA onboard Cluster are available and the penetrating electron background can be identified in the energy-time spectrograms as a sharp increase in the counting rates appearing simultaneously in all energy channels.

At the same time, the applicability of such a method meets with a difficulty when HIA data are not available, as has occurred during the later Cluster years. Moreover, the Double Star mission was a rather short mission. Regardless of the absence of HIA data, we suggest a new approach to define the locations of radiation boundaries using the background information when only the CODIF instrument data are in use.

Despite its designed lifetime of 2 years, Cluster has been providing the data for more than 20 years now. As of October 2020, its mission has been extended, at least, until the end of 2022. The new approach presented in the current paper aims towards the full usage of this unprecedented repository of data to reveal the radiation belts structure and dynamics. Section 2 briefly describes the instrumentation and data used in the paper. A new approach to define the locations of radiation belts boundaries using only CODIF data together with further applications of our previously developed method when both HIA and CODIF data are available are demonstrated in Section 3. Two time periods are analyzed in detail as two examples when a storage ring was clearly observed on Cluster (both HIA and CODIF instruments) and Double Star (HIA instrument) data on July–August 2007 and only on Cluster CODIF data on September–October 2012. We discuss both methods and draw conclusions in Section 4. The wider purpose of the paper is to demonstrate how to turn the instrument background into scientifically valuable data.

2. Instrumentation

The Cluster mission was launched in 2000 and it consists of four identical spacecraft on similar elliptical polar orbits with an initial perigee at about $4 R_E$ ($R_E = 6371$ km is the Earth's radius) and an apogee at $19.6 R_E$ (Escoubert et al., 2001). During perigee passes, Cluster traverses the inner magnetosphere providing its latitudinal profiles

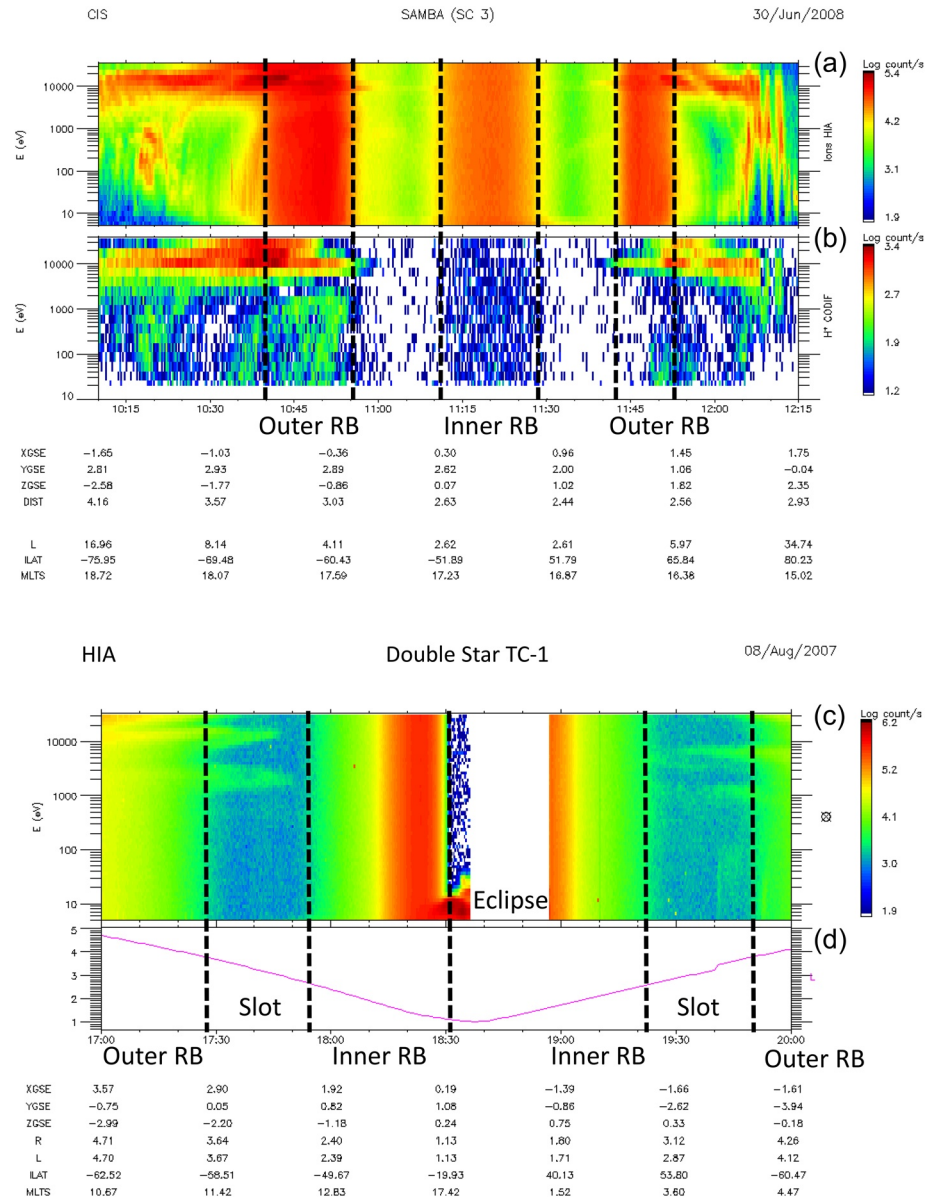


Figure 1. Example of boundaries (dashed vertical lines) of outer and inner radiation belts based on the measured background seen in the energy versus time ion spectrograms in counts/second by the Cluster (a) HIA and (b) CODIF instruments on June 30, 2008, and (c) Double Star TC-1 HIA energy-time spectrogram in counts/second together with (d) L-values on August 8, 2007 (reproduced from (Ganushkina et al., 2011)).

almost along the same flux tube (Dandouras, 2013; Dandouras et al., 2005, 2009) and covering all magnetic local times (MLTs) when crossing the equator due to the annual precession of its orbit.

The Cluster orbit perigee moved closer to the Earth, from about $4 R_E$ in the year 2000 to about $1.3 R_E$ in the year 2010 due to Sun–Moon gravitational perturbations and to maneuvers (Escoubet et al., 2015). In November 2009, the orbit period was reduced to about 54 hr 35 min due to the lowering of the apogees of the four Cluster spacecraft by about 5,000 km. The orbit inclination had deviated from its original 90° and the apogee moved to the Southern Hemisphere. In 2013, the perigee altitude increased again and apogee started returning back to the Northern Hemisphere. In 2017–2018, the gravitational perturbations resulted even in an increase of perigee up to $6\text{--}7 R_E$.

Table 1

List of Available Cluster and Double Star Observations of a Storage Ring During July–August 2007 Period With Dates Discussed in Detail Marked by Bold

Day	Month	UT interval	Satellite	Storage ring	MLT
2	July	1000–1300	Cluster	no	16.5–16.8
3	July	0600–0800	Double Star	no	14–20, 02–05
7	July	0500–0730	Cluster	yes	15.4–17.4
11	July	0600–0800	Double Star	yes, inbound	13–16, 03–05
13	July	1200–1500	Double Star	yes	12–14, 3–6
14	July	0800–1030	Cluster	yes	15–16
16	July	1630–2000	Cluster	unclear/yes	16
18	July	0100–0400	Double Star	yes	13–15, 4–6
19	July	0200–0500	Cluster	yes	15–16
19	July	0400–0700	Double Star	yes	13–15, 3–5
21	July	1130–1400	Cluster	yes/weak	15
21	July	1200–1300	Double Star	unclear	13–16
23	July	2000–2330	Cluster	no	15–16
24	July	2100–2400	Double Star	yes	12–14, 4–6
26	July	0600–0830	Cluster	yes	15–16
26	July	0100–0300	Double Star	yes	13–15, 3–5
27	July	0400–0600	Double Star	unclear	13–15, 3–5
28	July	1400–1730	Cluster	yes/weaker	15–16
31	July	2300–0230	Cluster	yes/weaker	15–16
2	August	0900–1200	Cluster	yes/weak	15
4	August	1700–2030	Cluster	no	15
7	August	0300–0600	Cluster	no	14–15
7	August	1400–1700	Double Star	no	11–14, 2–4

CODIF and HIA are two complementary spectrometers of the Cluster Ion Spectrometry (CIS) experiment with the time resolution of 4 s (one spacecraft spin) (Rème et al., 2001). The mass-resolving spectrometer CODIF provides the three-dimensional ion distribution functions for the major magnetospheric species (H^+ , He^+ , He^{++} , and O^+), with energies from ~ 25 eV/e to about 40 keV/e. The CODIF instrument combines ion energy per charge selection, by deflection in a rotationally symmetric toroidal electrostatic analyzer, with a subsequent time-of-flight analysis. An MCP (microchannel plate) detector ring is used to detect both the incoming ions and the secondary electrons, provided by the time-of-flight system. The detector ring is segmented in 16 anodes, each anode covering 22.5° . These anodes are grouped in two sections of 180° each, and only one of the two sections is operated at a time. The HIA sensor does not provide mass resolution but instead detects ions in the energy range of 5 eV/e to 32 keV/e with an angular resolution of 5.6° . The magnetic field data are from the FGM (Fluxgate Magnetometer) experiment (Balogh et al., 2001).

The Double Star TC-1 was the joint mission of the European Space Agency (ESA) and China National Space Administration (CNSA) launched into an elliptical orbit of 1.09 – $13.4 R_E$ with 28.5° inclination in 2004 (Liu et al., 2005). It reentered the atmosphere on October 2007. The Cluster and Double Star orbits were in almost the same meridian. The HIA instrument on board the Double Star TC-1 spacecraft, which was nearly identical to the CIS HIA sensor on board Cluster, measured the three-dimensional ion distribution functions without mass discrimination with energies between 5 eV/q and 32 keV/q (Rème et al., 2005). The magnetic field data come from the FGM experiment (Carr et al., 2005).

3. Turning Instrument Background Into Science Data

3.1. Boundaries of the MeV Radiation From keV Measurements by Both Cluster CIS HIA and CODIF and Double Star HIA

3.1.1. Method to Determine the Boundaries of Radiation Belts

Decreasing of perigee resulted in Cluster entering deep in to the radiation belts region, where MeV particles can penetrate through the walls of electrostatic-analyzer plasma instruments and directly affect their MCP detectors. Such penetrating particles induce a counting background that can be used to identify the presence of these very energetic populations (Delory et al., 2012; Ganushkina et al., 2011). Figure 1 (see Figures 1 and 4 in Ganushkina et al., 2011) presents example energy-time spectrograms in counts/second measured by (a) HIA and (b) CODIF instruments on June 30, 2008 with Cluster going as low as $L = 2.6$ to illustrate the method to identify the inner and outer radiation belt boundaries out of the background counts. The counts appearing simultaneously in all energy channels as seen in HIA spectrogram strongly indicate that they come from the penetrating particle background, insensitive to the particle energy selection by the electrostatic analyzer. Entering and leaving the outer and inner radiation belts which can be seen in the presence or absence of the background counts in all energy channels provide the locations of the boundaries of the outer and inner radiation belts (marked by dashed vertical lines). The background seen in CODIF spectrogram provides additional information but it cannot be used in a similar way as HIA spectrogram for determining the boundaries. The double signal coincidence technique used in CODIF to eliminate most of the penetrating particles results in the reduced background without clear appearance of simultaneous counts in all energy channels. Figure 1 demonstrates an example of an energy-time spectrogram (c) in counts/second measured by the Double Star HIA instrument on August 8, 2007 together with (d) L-values. The white gap on the spectrogram corresponds to the spacecraft being in eclipse. Since the background measured by the Double Star HIA instrument is rather similar to that of Cluster HIA, the same method was applied to identify the boundaries. When Double Star leaves the outer belt moving inbound, it crosses the inner boundary of the outer radiation belt. It then detects the slot region between this boundary and the outer boundary of the inner radiation belt. Close

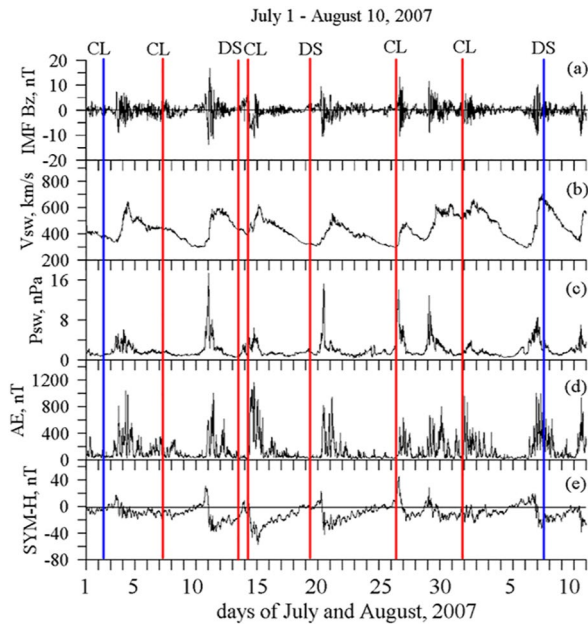


Figure 2. Overview of solar wind and geomagnetic activity during the July 1–August 10, 2007 period with vertical lines marking selected times for Cluster and Double Star when a storage ring was observed (red) or not (blue).

Table 1 presents the list of all days with UT intervals when data were available, listing whether or not the boundaries of storage ring were noticeable and MLTs crossed by the satellites. The dates of observations that we discuss in more detail in the present paper are marked bold. Due to the type of the orbit, Cluster crossed the inner magnetosphere regions at 14–16 MLT on both inbound and outbound passes for all the days. Double Star was at 12–16 MLT on the inbound and at 02–06 MLT on the outbound passes.

The overview of the solar wind and geomagnetic activity during the period of interest from July 1 to August 10, 2007 is presented in Figure 2. High resolution (5 min) data were obtained from OMNIWeb (<https://omniweb.gsfc.nasa.gov/>). Variations of (a) IMF B_z , (b) solar wind speed V_{sw} , (c) solar wind dynamic pressure P_{sw} are shown together with the (d) AE, and (e) SYM-H indices.

Figures 3–6 present the sequence of selected measurements from Cluster and Double Star for the first half of July 2007 when the storage ring has appeared. Figures 8–10 show the selected measurements from Cluster and Double Star for the second half of July 2007 and the beginning of August 2007 when the storage ring has disappeared. The corresponding times are marked with bold font in Table 1 and with vertical solid lines in Figure 2.

Each plot of Cluster data (data from C3 satellite) in Figures 3, 4, 6, 8, and 9 shows in the top panel the energy-time ion spectrogram of counts per second from CIS HIA instrument where entering and leaving the regions with penetrating electron flux (>2 MeV for Cluster) can be identified as a sharp increase/decrease in the counting rates appearing/disappearing simultaneously in all energy channels.

The next panel presents the energy-time H^+ spectrogram of counts per second measured at CIS CODIF instrument. The CODIF instrument is the time-of-flight ion mass spectrometer with onboard processing which uses the detection of two signals, that is, a “start” signal and a “stop” signal separated in time by a valid time-of-flight interval (corresponding to the ion velocity) to validate an ion detection. This double signal coincidence technique helps in eliminating most of the penetrating particles, which produce only “single” signals, substantially reducing the background “ion counts” in the radiation belts. While the background can be still seen, the CODIF energy-time H^+ ion spectrograms are not best suited for the identification of the radiation belt boundaries.

to its perigee, Double Star leaves the inner belt (inner boundary of the inner radiation belt). When moving outbound, the outer boundary of the inner belt and the inner boundary of the outer belt are again crossed.

The Double Star data plot reveals also another feature: as seen in the spectrogram, when the spacecraft exits the inner belt and approaches perigee, and before the data gap due to the eclipse, the HIA instrument detects the ionospheric particles as a very intense population below 15 eV/q. This population is detected only in the tailward looking and in the dawnward looking sectors: this is due to the relative motion of the spacecraft with respect to the ambient plasma ($V_x < 0$ and $V_y < 0$ for the spacecraft) which “scoops” the cold plasma into the instrument.

We employ the same method of determining the boundaries of radiation belts from the background measurements on the keV instruments not covering the MeV energies of the radiation belts for identifying not only usually well-observed locations of the outer and inner belts but temporal boundaries of the storage ring.

3.1.2. Example Event on July–August 2007

During the first event on July–August 2007, signatures of a storage ring were clearly visible. This event was selected from the previously analyzed (Ganushkina et al., 2011) periods of Cluster data (April 2007–June 2009) and of Double Star data (May 15–28 September 2007). Both Cluster CIS HIA and CODIF data were available with Double Star HIA data in addition.

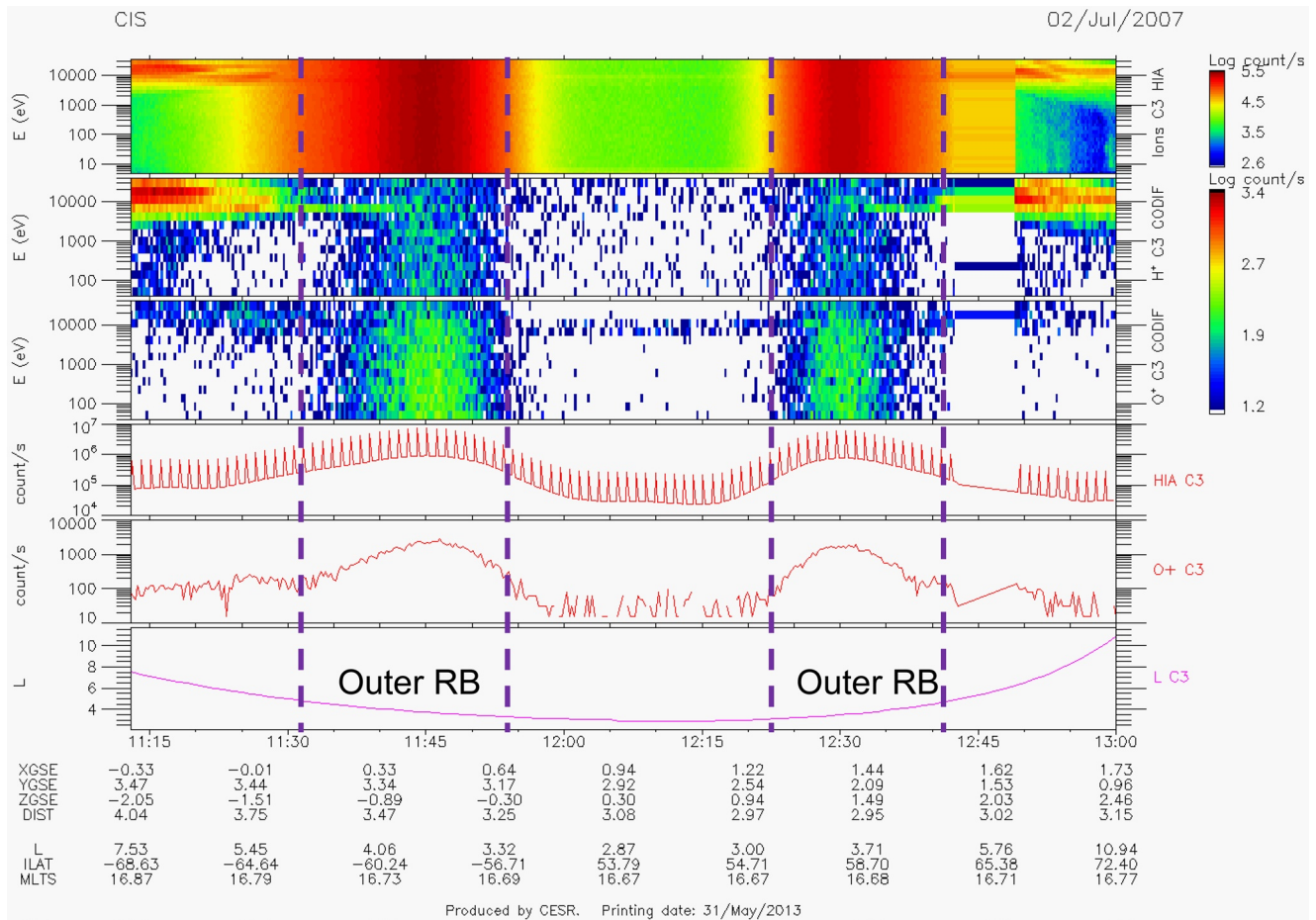


Figure 3. Cluster CIS data, July 2, 2007: energy-time spectrograms of counts/second for (top panel) ions from CIS HIA instrument, (second panel) H⁺ and (third panel) O⁺ ions from CIS CODIF instrument, integrated over all energies counts/second of (fourth panel) HIA ions and (fifth panel) CODIF O⁺ ions with (bottom panel) L values which Cluster crossed. The spikes in fourth panel are data artefact. Regions of outer radiation belts are marked by vertical dashed lines. No storage ring, intense radiation belt.

A partial exception to this is the O⁺ ion counts, shown in the next panel (third from the top). Due to the greater time-of-flight of these heavy ions (smaller velocity for a given energy), the valid time window for the detection of both a “start” signal and a “stop” signal is longer. This increases the probability of detecting during this time window two uncorrelated penetrating particles generating two signals (one each), one penetrating particle mimicking a “start” signal and the other mimicking a “stop” signal, and generating thus a false (background) O⁺ ion count. The fourth panel from the top presents the HIA ion counts per second integrated over all energies, whereas the fifth panel shows CODIF O⁺ counts per second integrated over all energies. The spikes on the plot are data artifact. Variations in CODIF O⁺ counts reflect the appearance of the background as seen in HIA spectrograms. The sixth and last panel in the bottom contains the L-values which Cluster crossed.

The top panel at each plot of Double Star measurements in Figures 5, 7, and 10 contains instrument operation data (instrument mode and MCP high-voltage settings), whereas the following five panels show ion energy-time spectrograms in counts per second units. The first four of them show ions arriving in the 90° × 180° sector with a field-of-view pointing in the sun (second panel from the top), dusk (third panel), tail (fourth panel), and dawn (fifth panel) direction respectively, whereas the sixth panel shows the omni-directional data. These allow the confirmation of the isotropic nature of the plasma outside the background areas of the radiation belts. Note that, due to a thicker shielding on Double Star than on Cluster, the background due to the penetrating particles is reduced allowing to identify the plasma populations even in the outer radiation belt and in the storage ring. This is not, however, the case in the inner belt, where the count rates due to the penetrating particles are extreme and saturate

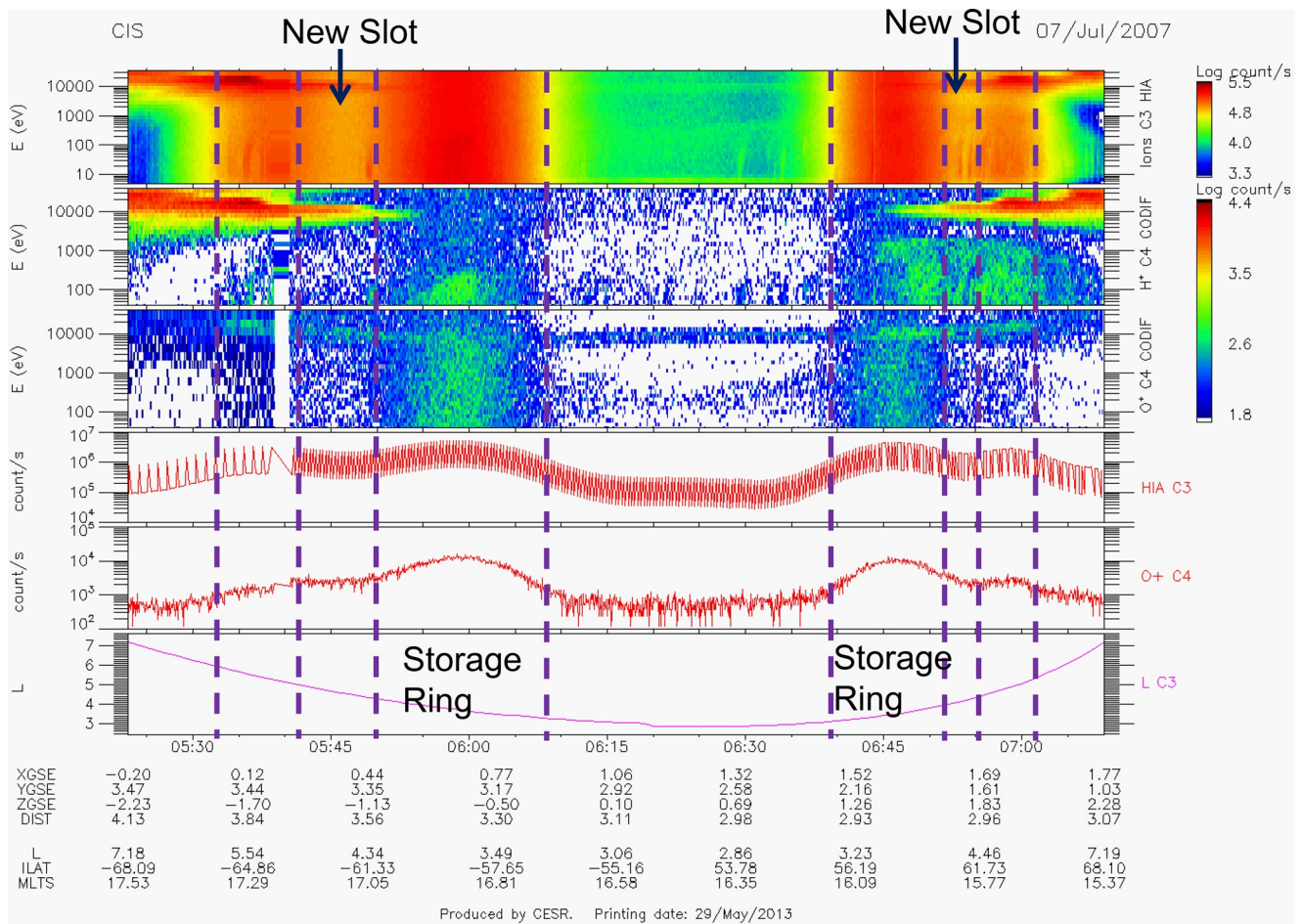


Figure 4. Cluster CIS data (similar to Figure 3), July 7, 2007: Appearance of storage ring.

the detector. The data gap, at the middle of the inner belt, is due to a loss of data acquisition when the satellite gets in the Earth's shadow (loss of Sun-reference pulse). The seventh panel presents the plasma density as calculated from the measured ion distribution functions. Outside the radiation belts, for example, in the slot region, this gives the density of the ion populations that are in the instrument energy range (5 eV/q–32 keV/q). However, in the areas where background due to penetrating particles is present, this density value is artificially boosted by the penetrating particle counts. The bottom, eighth panel shows the L-shell value evolution.

We will analyze Figures 2–10 together with Table 1 simultaneously when describing the appearance, persistence and disappearance of a storage ring during the July–August 2007 time period as seen in Cluster and Double Star spectrograms. As can be seen in Figure 2, the beginning of July (July 1–3) was rather quiet. Cluster observations on July 2, 11–13 UT (marked as blue vertical line in Figure 2) did not contain any indications of a storage ring presence (Figure 3). We can see Cluster entering and leaving the outer radiation belt as it is shown in the background counts in the spectrograms and in the peaks of the integrated over all energies HIA ion and CODIF O⁺ counts.

During the period of July 3–6, large oscillations in IMF B_z , a gradual increase of V_{sw} to 640 km/s indicated the occurrence of a small CIR (Corotating Interaction Region) storm with HSS (high speed stream) feature. The first signs of a storage ring appeared (Figure 4) on July 7, 05–08 UT (red vertical line in Figure 2). A new slot was formed in the HIA spectrogram with the reduced background counts between two areas with the increased background counts. CODIF spectrograms are less definite but both integrated over all energies HIA ion and CODIF O⁺ counts curves show two peaks corresponding to the increased background counts with a dip between them corresponding to a newly formed slot. The background counts at distances closer to Cluster perigee are the

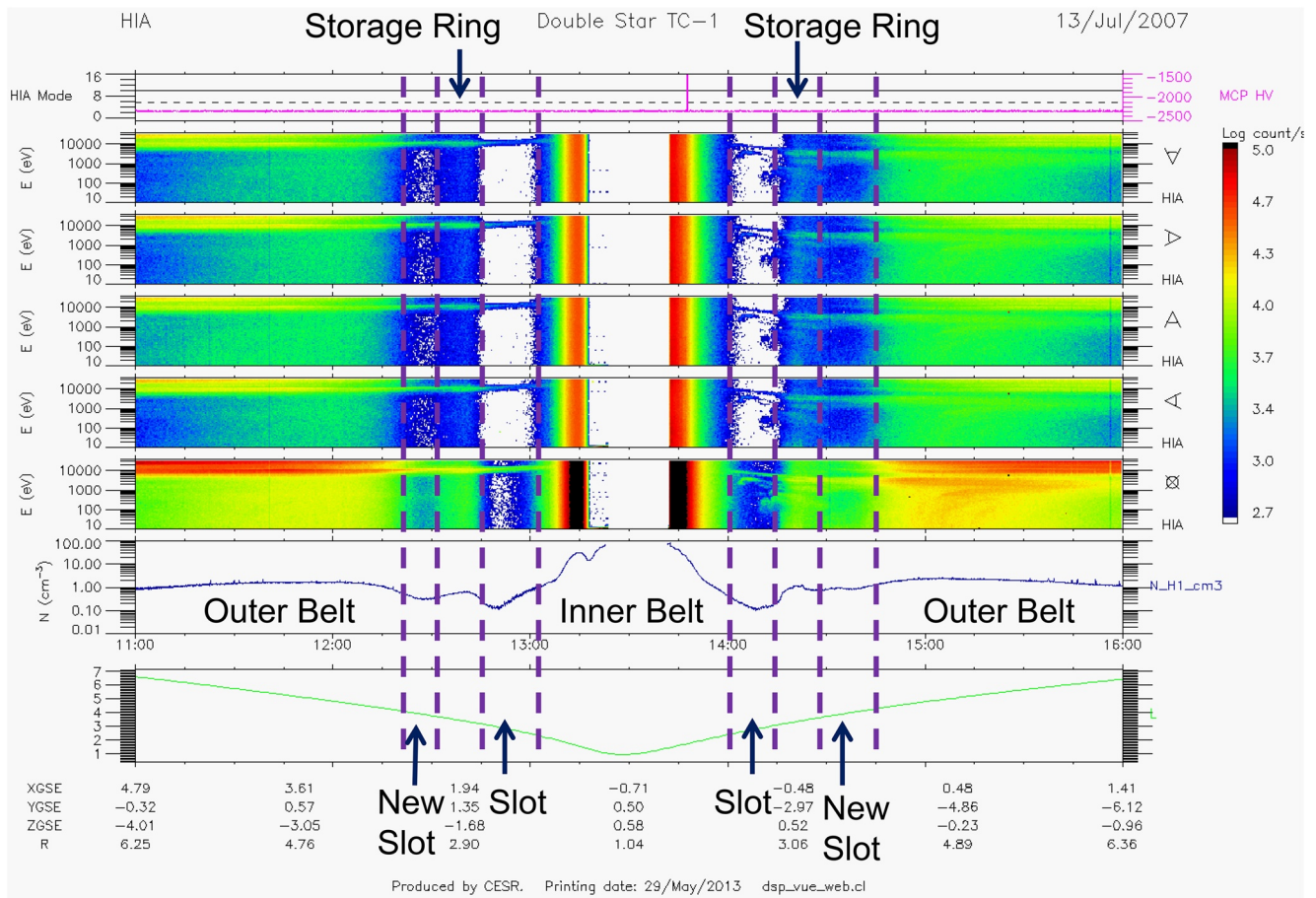


Figure 5. Double Star HIA data, July 13, 2007: (top panel) instrument operation data as instrument mode and MCP high-voltage settings, ion energy-time spectrograms in counts/second with ions arriving in the $90^\circ \times 180^\circ$ sector with a field-of-view pointing in the sun (second panel from the top), dusk (third panel), tail (fourth panel), and dawn (fifth panel) direction respectively with omni-directional data (sixth panel), (seventh panel) plasma density as calculated from the measured ion distribution functions, and (eighth panel) L-shell values. The data gap is due to a loss of data acquisition when the satellite gets in the Earth's shadow. Regions of radiation belts are marked by vertical dashed lines. Clear storage ring.

indicators of a storage ring presence. If this storage ring was formed due to the small CIR storm described above, Cluster observed it 3.5 days after the storm maximum.

End of July 10 when IMF B_z reached about -10 nT was the initial phase of a small CME storm with SYM-H dropping to -30 nT in the beginning of July 11. Double Star observed a clear signature of a storage ring (Table 1, data only from inbound pass, not shown) during the 06–08 UT interval which was at around the main phase of the storm. Very distinct signatures of a storage ring were seen on Double Star at 12–15 UT of July 13 (Figure 5). Several boundaries are seen in Figure 5: the inner boundary of the outer radiation belt (first vertical dashed line on Double Star inbound pass) and outer boundary of the inner radiation belt (last vertical dashed line on Double Star inbound pass) and the same boundaries in the reverse order on the outbound pass. In addition to the boundaries described above, in Figure 5, we see a new, second slot formed between the inner boundary of the outer radiation belt and a new area of background counts. This new area is the storage ring seen in Double Star data, especially distinct in the omni-directional spectrogram (third panel from the bottom). The plasma density presented at the second panel from the bottom shows a clear increases due to penetrating particles when Double Star enters the radiation zones and decreases when it goes into slot regions. The storage ring was observed at the maximum of a small CME storm and after two days of storm recovery. It is hard to say whether we see the same, previously formed storage ring after the small CIR storm on July 4 or the new one formed at the small CME storm.

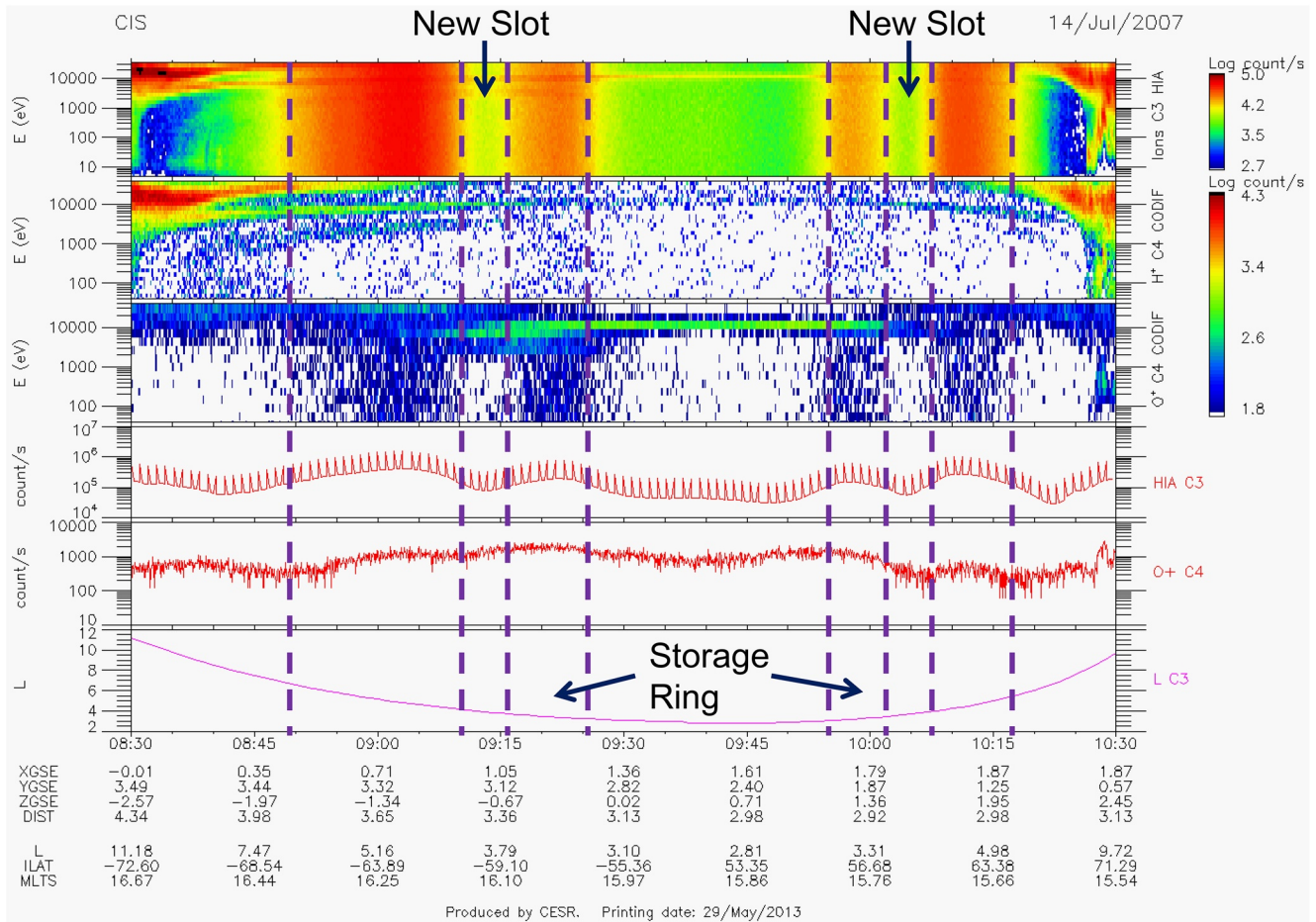


Figure 6. Cluster CIS data (similar to Figure 3), July 14, 2007: Clear storage ring.

The next CME-type storm occurred on July 14 with an initial southward turning of the IMF B_z at around 09 UT (-11 nT at about 18 UT). Cluster observed very clear signatures of a storage ring during 09–10 UT on July 14, right at the beginning of the main phase of the storm (Figure 6). We can see a very distinct new slot between the inner boundary of the outer radiation belt and outer boundary of the storage ring. The next two observations (Table 1, data not shown) also contained storage ring signatures. While July 19 was a rather quiet day, Cluster observed clear signatures of a storage ring during 03–04 UT (data not shown) and Double Star saw them, too, during 05–08 UT on that day (Figure 7) with a second slot and a new area of background counts. After that, no clear signatures of a storage ring were seen until July 24 when Double Star (data not shown) spectrograms showed the distinct increases in the background counts representing the presence of a storage ring. Two days later on July 26, while geomagnetic conditions were still not disturbed, Double Star (data not shown) still saw a storage ring present on 01–03 UT and later Cluster observed still clear signatures on 06–0830 UT (Figure 8).

Cluster observed storage ring features on the end of July 31–beginning of August 1, 2300–0230 UT (Figure 9), but they were considerably weaker than those on August 2, 09–12 UT (data not shown). Observations from Cluster on August 4, 17–2030 UT, and August 7, 03–06 UT (data not shown), and Double Star on August 7, 14–17 UT (Figure 10, the thin vertical stripes in the spectrograms are telemetry glitches), did not show any storage ring signatures.

The conducted analysis of the locations of boundaries determined from the background counts is able to provide the L-values for each boundary detected during the July–August 2007 event (Figure 11) on both satellites. On the inbound pass, the satellites first cross the outer boundary of the outer belt (blue rhombuses) which locations varies from 5 to 8 in L being on average at $L = 6$. The inner boundary of the outer belt is marked by the blue circles (located at about $L = 4$), the outer boundary of the storage ring is marked by the red circles and the gap between

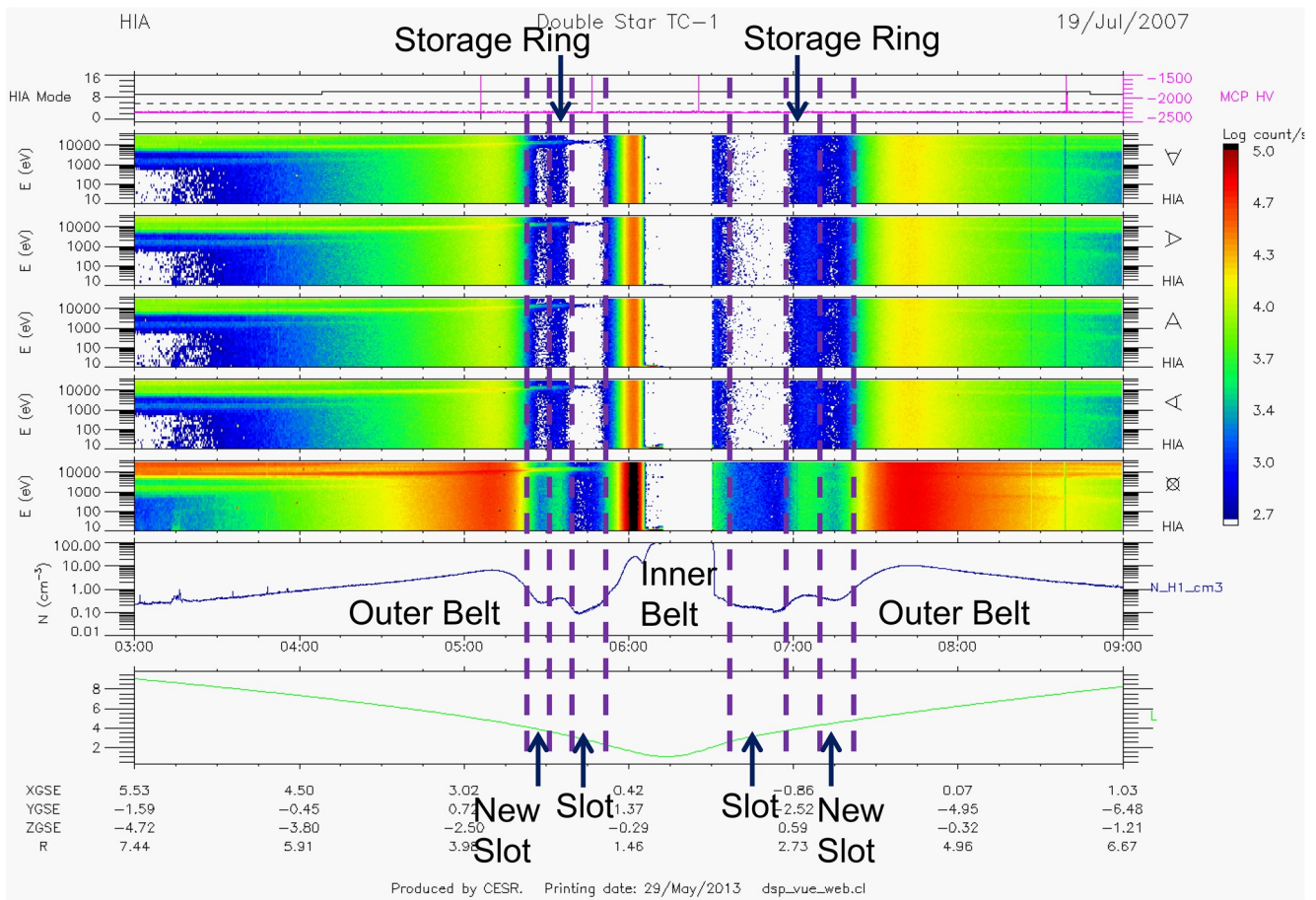


Figure 7. Double Star HIA data (similar to Figure 5), July 19, 2007: Clear storage ring.

them is the new slot. Red triangles depict the locations of the inner boundary of the storage ring. The mean width of the new slot and new storage ring in L is about 0.3–0.5. So, the storage ring is usually located at Ls between 3 and 4. Thus, background information can be of high use, especially, if no actual particle data are available.

3.2. Boundaries of the MeV Radiation From keV Measurements From Cluster CIS CODIF Only

3.2.1. Adaptation of Method to Determine the Boundaries of Radiation Belts

As was presented above, if the data from the simple electrostatic analyzer instrument HIA onboard Cluster and Double Star are available, the radiation belt boundaries can be identified in the energy-time spectrograms as a sharp increase in the counting rates appearing simultaneously in all energy channels. No data from the Double Star spacecraft, however, have been available after October 2007. Since October 2012, HIA instrument operations onboard Cluster have been reduced to 1 hr per orbit due to an instrument issue. For the events where no HIA data were available (HIA instrument switched off onboard Cluster), we have to apply a new method here, so as to use the data of only the CODIF instrument. As was mentioned in the descriptions of CODIF spectrograms shown in in Figures 3, 4, 6, 8, and 9, the double signal coincidence technique used in the CODIF instrument significantly reduces the background counts. Energy-time ion spectrograms from CODIF alone cannot be directly used in a similar way as HIA spectrograms.

The O⁺ ion counts, due to their longer time-of-flight as compared to H⁺ and longer time window for both the “start” and “stop” signal, have increased probability to detect the generated false background as was explained in Section 3.1.2. When defining the boundary position from CODIF spectrograms, we analyze the changes in O⁺ ion counts/sec with time $\frac{\Delta \text{counts}}{\Delta t}$ for all 31 energy channels step by step in time. Whenever possible, we determine the

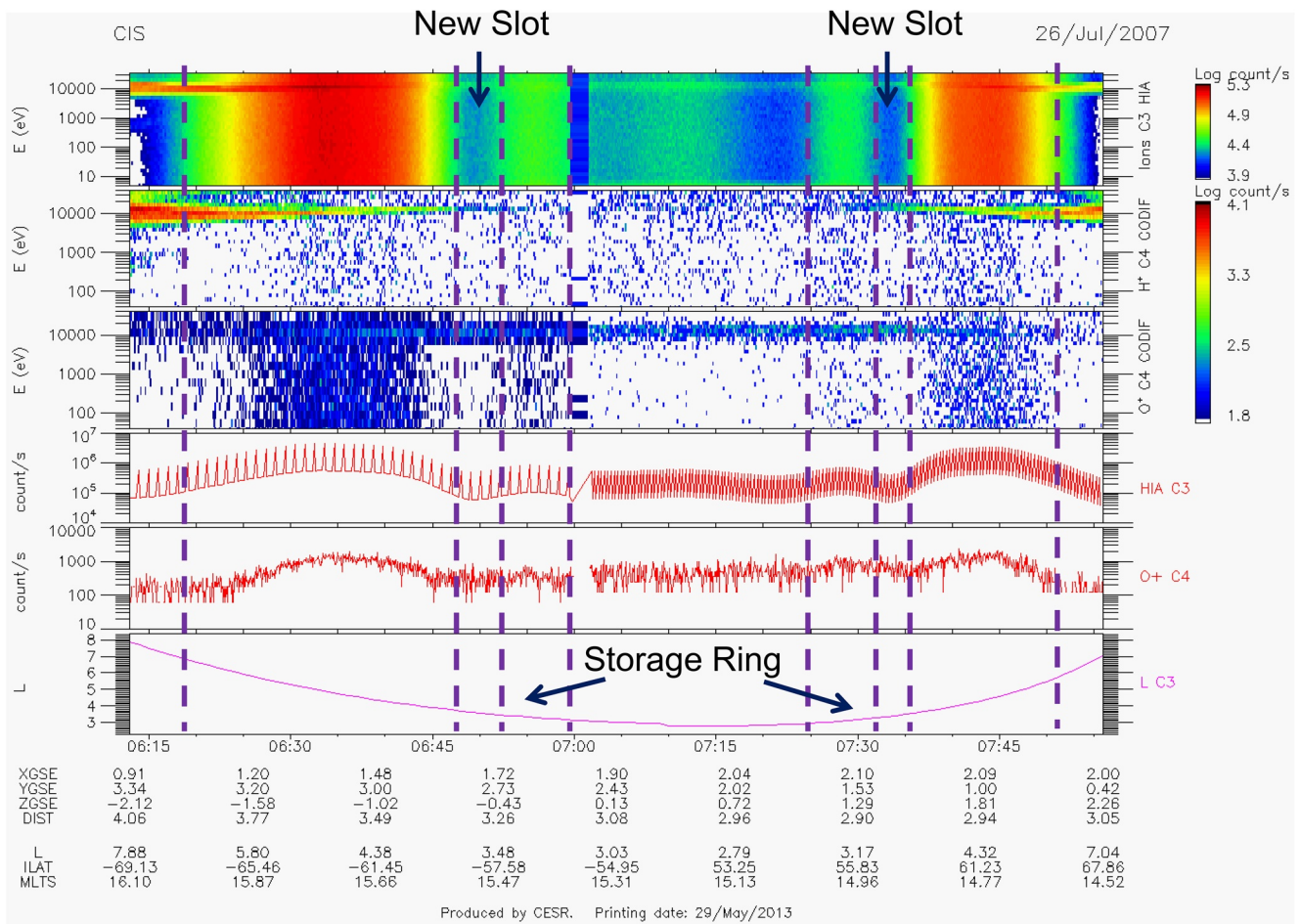


Figure 8. Cluster CIS data (similar to Figure 3), July 26, 2007: Clear storage ring.

first time moment, when the $\frac{\Delta \text{counts}}{\Delta t}$ is the largest and the same for all energy channels (sharpest gradient) and put a boundary there. We compare two time steps before and two time steps after of each time moment. We always conduct a visual inspection of the defined boundary locations.

In the new approach, additional information for penetrating particles comes from the CODIF full telemetry data set, which besides the valid ion detection events (“start” signal plus “stop” signal plus valid detection position for each event, i.e., valid ion detected) includes also count rates of “single” events. These are separate counters that register (a) the total of the “start” signals detected, independently of whether a start signal was accompanied by a stop signal or not (“start” rates), (b) the total of the “stop” signals detected, independently of whether a stop signal was preceded by a start signal or not (“stop” rates), and also (c) the “non-valid” event rates (Kistler et al., 2013). These additional data streams are not energy dependent but rather summed over all energy channels and look directions.

“Start” and “stop” rates give thus each a measure of the sum of the detected ions (valid detections), plus the ions that generated only a “start” or only a “stop” signal respectively (due to the finite detection efficiency of the MCPs), plus the penetrating particles. In the presence of penetrating particles the “start,” “stop,” and “non-valid” event rates increase, but this increase is not accompanied by a corresponding increase of the valid events that are shown in the energy-time spectrograms, particularly for the light ions as H⁺. To define the boundary position from telemetry signals, we follow the evolution of the telemetry counts/sec with time $\frac{\Delta \text{counts}}{\Delta t}$ for all 3 signals described above. We determine all the time moments, when the $\frac{\Delta \text{counts}}{\Delta t}$ changes its sign and attribute them with local minima and maxima. The same procedure is applied to CODIF O⁺ counts per second integrated over all energies. It is thus the combined information from these CODIF data, that is, O⁺ ion count rates, “start” count rates and

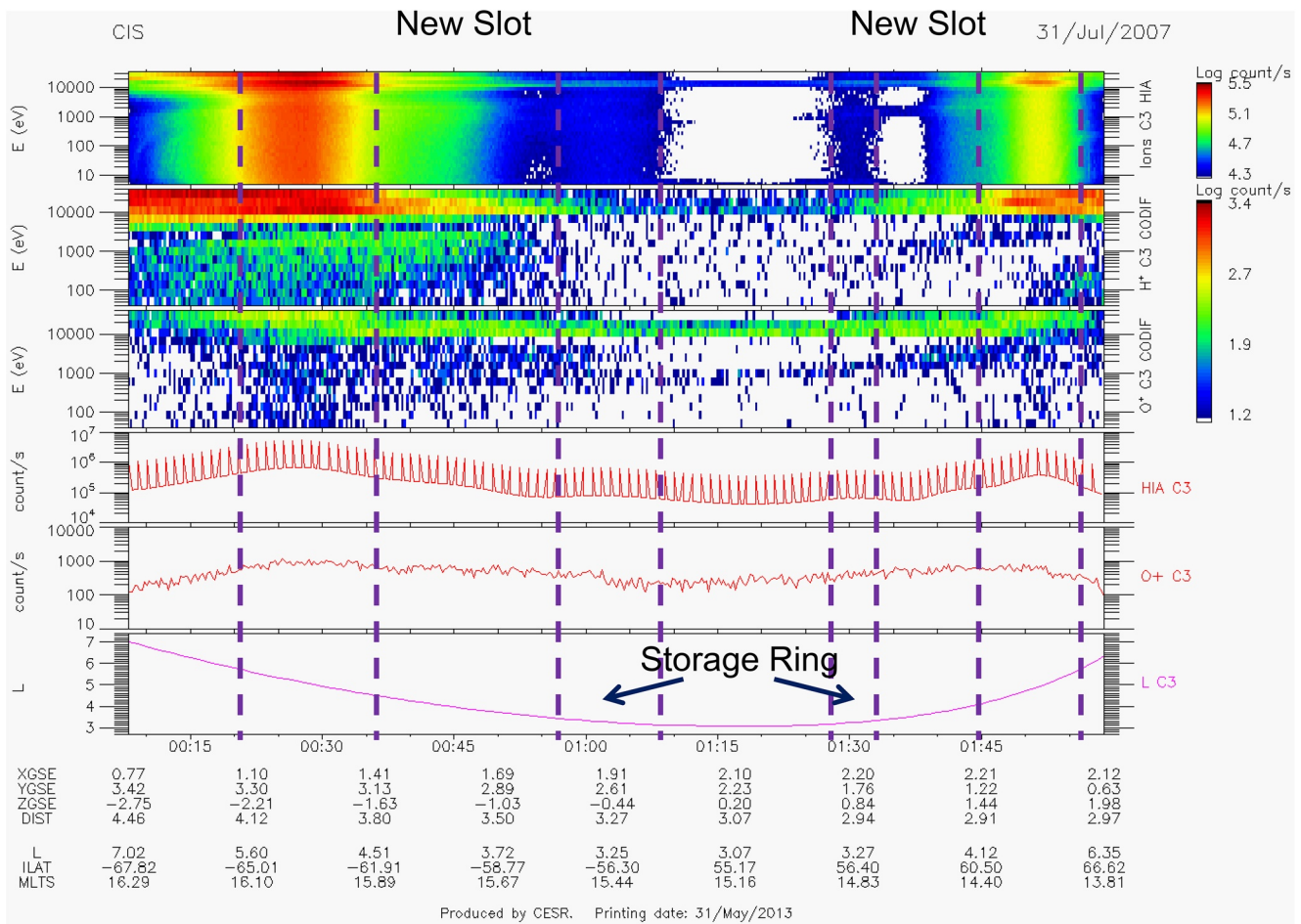


Figure 9. Cluster CIS data (similar to Figure 3), July 31, 2007: Weaker storage ring.

“non-valid” event count rates that is used here to identify and locate the boundaries of the radiation belts and of the storage ring. It includes the quantitative determination of directions of changes in counts gradients along the orbit and qualitative visual inspection of all the available measurements taking also into account the exact locations of Cluster in the magnetosphere (L, latitude etc.). This is demonstrated below for the September–October 2012 event, an interval with a documented presence of a storage ring by Baker et al. (2013).

3.2.2. Example Event on September–October 2012

As an example to demonstrate the validity of the new approach to determine the boundaries of radiation belts when only Cluster CODIF data were available, the September–October 2012 period was selected which has been extensively analyzed starting with the Baker et al. (2013) study. Table 2 contains the list of available Cluster observations during the September–October 2012 period with corresponding UT intervals, presence or absence of storage ring features, determined L-values and MLT sectors for storage ring (when present). Not many observations were available from Cluster during that period but the presence of a storage ring detected from them is in agreement with what was shown in Baker et al. (2013) (see their Figure 3a). According to Baker et al. (2013), a “storage ring” of high-energy electrons emerged after September 2 (Cluster saw first signatures of a storage ring on September 8) and disappeared on October 1 (Cluster did not observe any clear signatures of a storage ring starting from October 1).

Figure 12 presents the overview of solar wind and geomagnetic activity during the September 1–15 October 2012 period with vertical lines marking times when Cluster observed the storage ring (red), the observed storage ring was weak (dashed red) and not observed (blue). As in Figure 2, the time series of (a) IMF B_z , (b) solar wind speed V_{sw} , (c) solar wind dynamics pressure P_{sw} are shown together with (d) AE and (e) SYM-H indices. An

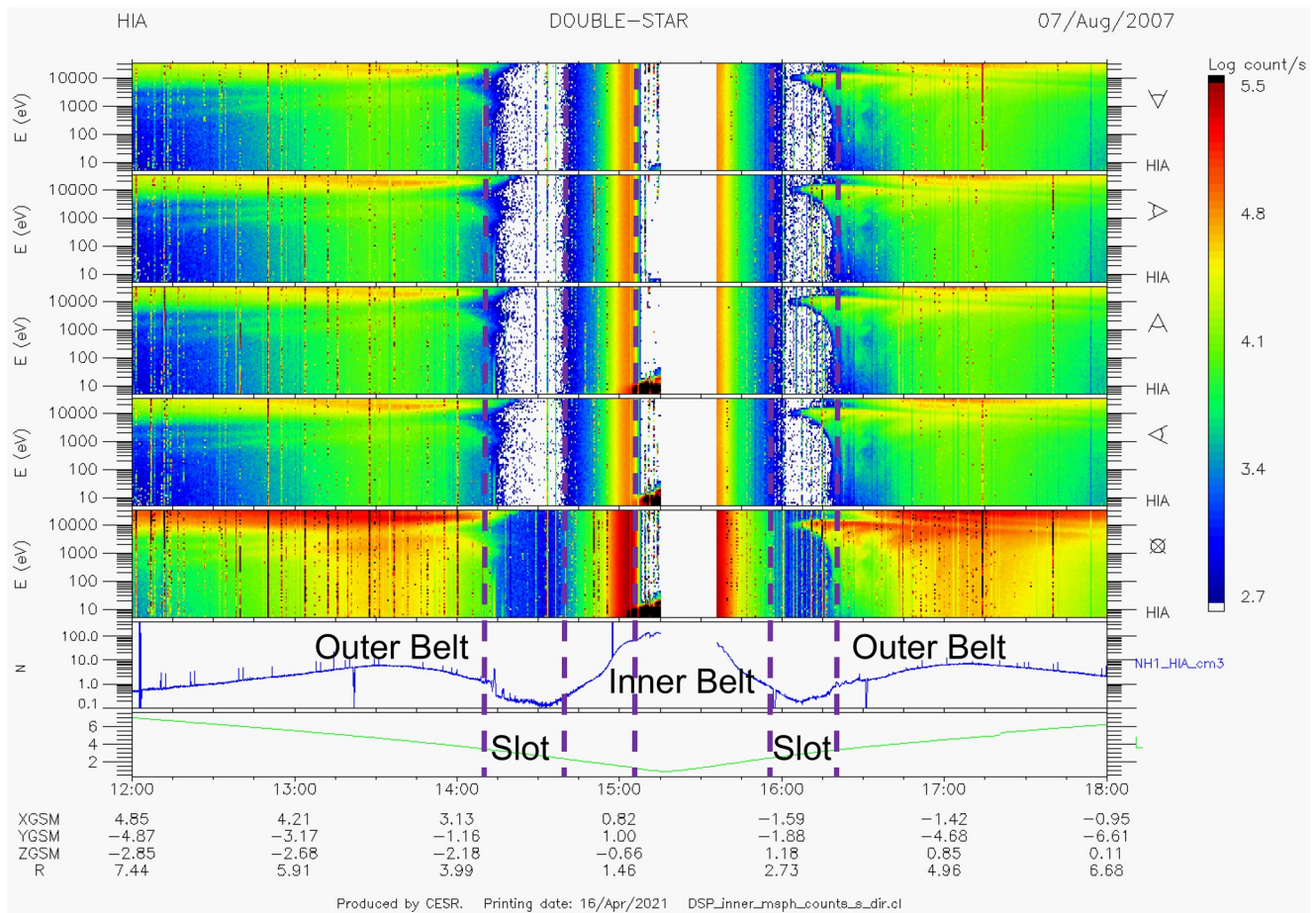


Figure 10. Double Star HIA data (similar to Figure 5 but without instrument operation data), August 7, 2007: No storage ring.

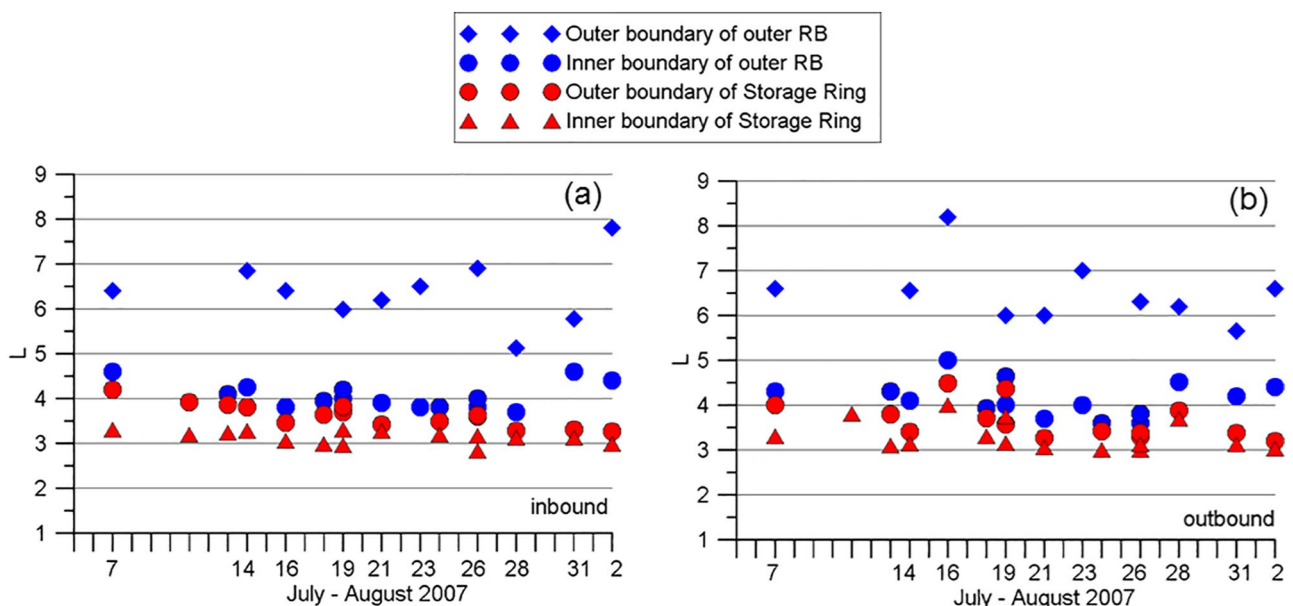


Figure 11. L-values for radiation belt boundaries determined from the background counts from (a) inbound and (b) outbound passes of both Cluster and Double Star satellites during the July–August 2007 event.

Table 2
List of Available Cluster Observations During the September–October 2012 Period With Dates Discussed in Detail Marked by Bold

Day	Month	UT interval	Storage ring (SR)	L_{SR}	MLT_{SR}
2	September	0300–0600	no		
8	September	2100–0100	yes	3.0–3.4	0840–0815
11	September	0300–0800	yes	2.9–3.3	0835–0810
15	September	1600–2000	yes	3.0–3.4	0810–0745
17–18	September	2200–0200	yes	3.0–3.4	0810–0745
20	September	0500–0800	yes, weak	3.1–3.4	0750–0730
22	September	1100–1500	yes, very weak		
1	October	1230–1530	no		
3	October	1830–2200	no		
6	October	0100–0400	no		
8	October	0600–1000	no		
10	October	1200–1700	no		
12	October	1800–2300	no		

interplanetary shock wave has passed on September 3 which can be seen as a sharp increase in V_{sw} (Figure 12b) and change in the IMF B_z (Figure 12). The appearance of a new population of relativistic electrons at a around $L = 4$ was associated with the high value of V_{sw} on September 5. Cluster saw signatures of a storage ring on four passes (from September 8 to September 17). Another high speed solar wind stream was observed on September 20–21 which was also related to another period of high-energy electron flux (Cluster observed weaker storage ring on September 20 and 22). One more interplanetary shock wave passed on October 1st and SYM-H index dropped to -150 nT indicating the occurrence of a moderate geomagnetic storm (Figure 12e) but no signatures of a storage ring were observed.

We will concentrate on two time intervals of Cluster data in the present paper, September 11, 04–07 UT, and October 6, 0040–0430 UT. They are marked bold in Table 2. Figure 13 presents the observations on September 11 when the storage ring features were seen. Three upper panels show the energy-time spectrograms of fluxes of three ion species measured by Cluster CODIF instrument, H^+ , He^+ , and O^+ , respectively. The background counts on the H^+ spectrogram (Figure 13a) do not indicate any storage ring signatures. The same is true to the counts on He^+ spectrogram (Figure 13b). O^+ spectrogram provides the possibility to detect the background more clearly (Figure 13c). It is obvious from Figure 13d, where CODIF O^+ counts per second integrated over all energies are presented.

O^+ counts show an increase and a decrease at the UT interval from 0605 to 0617 which correspond to a storage ring. A storage ring is also present in the inbound pass as well, at around 0500 UT, however, on the outbound pass, the signature is more prominent, and therefore, we concentrate our analysis on the outbound pass only. The lower panels in Figure 13 present count rates for the (e) start signal, (f) stop signal and (g) start plus stop signals for “non-valid” event count rates without valid detection position. Panels (a)–(d)

present the particle counts transmitted in the “normal” science telemetry products with a high time resolution, whereas panels (e)–(g) show the “monitor rates” products, which are diagnostic telemetry products transmitted with a lower time resolution. We can see similar to Figure 13d peaks in all three count rates, so that it is possible to detect the location of the storage ring from these background counts (marked as vertical dashed lines). Cluster was going from dusk to dawn via noon during September–October 2012 event. Storage ring signatures were detectable mainly on the outbound pass, in the morning hours. L-values and MLTs for the observed storage ring background counts were obtained (shown in Table 2). At around 08 MLT, the storage ring is located between L-shells of 2.9 and 3.4 with the width ΔL of about 0.4.

Figure 14, in the same format as Figure 13, shows the Cluster CODIF energy-time spectrograms of fluxes of (a) H^+ , (b) He^+ and (c) O^+ , (d) O^+ counts per second integrated over all energies, and the count rates for CODIF (e) start signal, (f) stop signal, and (g) start plus stop signals for “non-valid” events for October 6. After September 22, Cluster did not see any signatures of the storage ring and October 6 is a good example of the absence of those signatures. Cluster saw a shrunken outer radiation belt (which was also noticed by Baker et al., 2013), and the outskirts of the inner belt but no peaks in the background counts which could indicate to a storage ring presence. Thus, combined O^+ ion counts and start, stop and “non-valid” event count rates from the CODIF instrument can be directly used to locate the permanent and transient features in the radiation belts, including their boundaries.

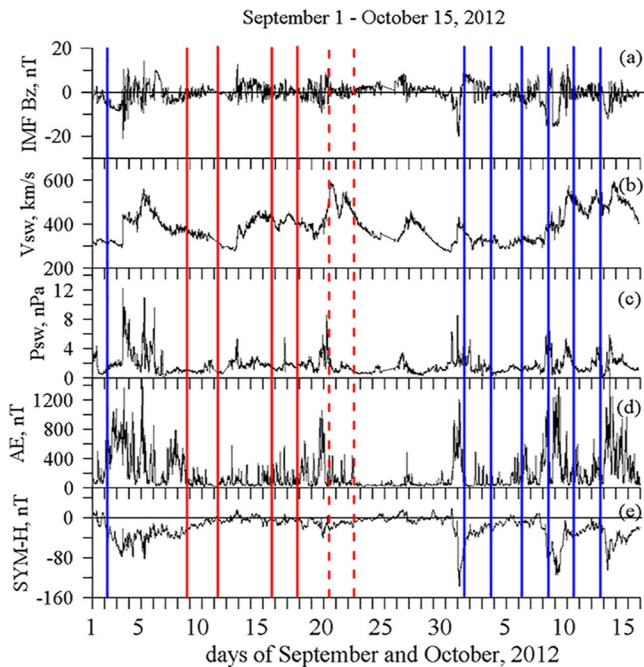


Figure 12. Overview of solar wind and geomagnetic activity during the September 1–October 15, 2012 period with vertical lines marking times when Cluster observed the storage ring (red), the observed storage ring was weak (dashed red) and not observed (blue).

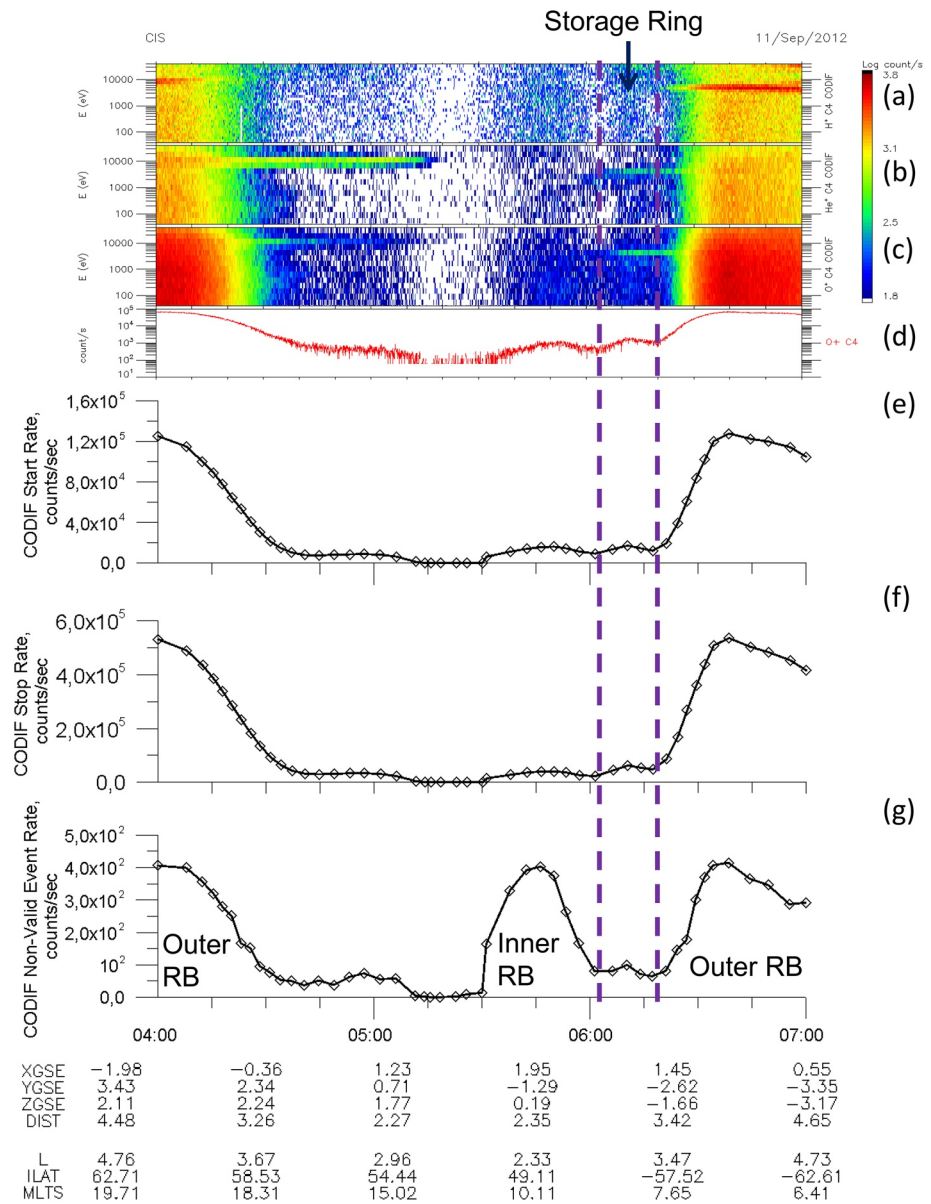


Figure 13. Presence of storage ring signatures as seen on Cluster CODIF data and in telemetry data (start, stop, and non-valid event rates) on September 11, 2012.

4. Discussion and Conclusions

This Technical Report on Methods paper has described the approach on how to turn the instrument background to scientifically valuable data. For this purpose, we have used the background counts due to penetrating energetic particles of radiation belts detected on Cluster CIS HIA and CODIF instruments. Appearance and disappearance of such background counts mark entering and leaving the radiation belts by the Cluster spacecraft. Thus, the locations of the boundaries of the outer and inner belts can be determined. In HIA spectrograms the counts are seen simultaneously in all energy channels and it is rather straightforward to define the boundaries. In the case when HIA measurements are not readily available, the double signal coincidence technique used in CODIF instrument does not allow to use the CODIF energy-time ion spectrograms alone for the same procedure of determining the locations of radiation belts. Therefore, a new approach was proposed in which CODIF full telemetry data is exploited. CODIF telemetry data employs separate counts that register “start,” “stop,” and “non-valid” signals which always increase in the presence of penetrating particles even when no corresponding increase are shown

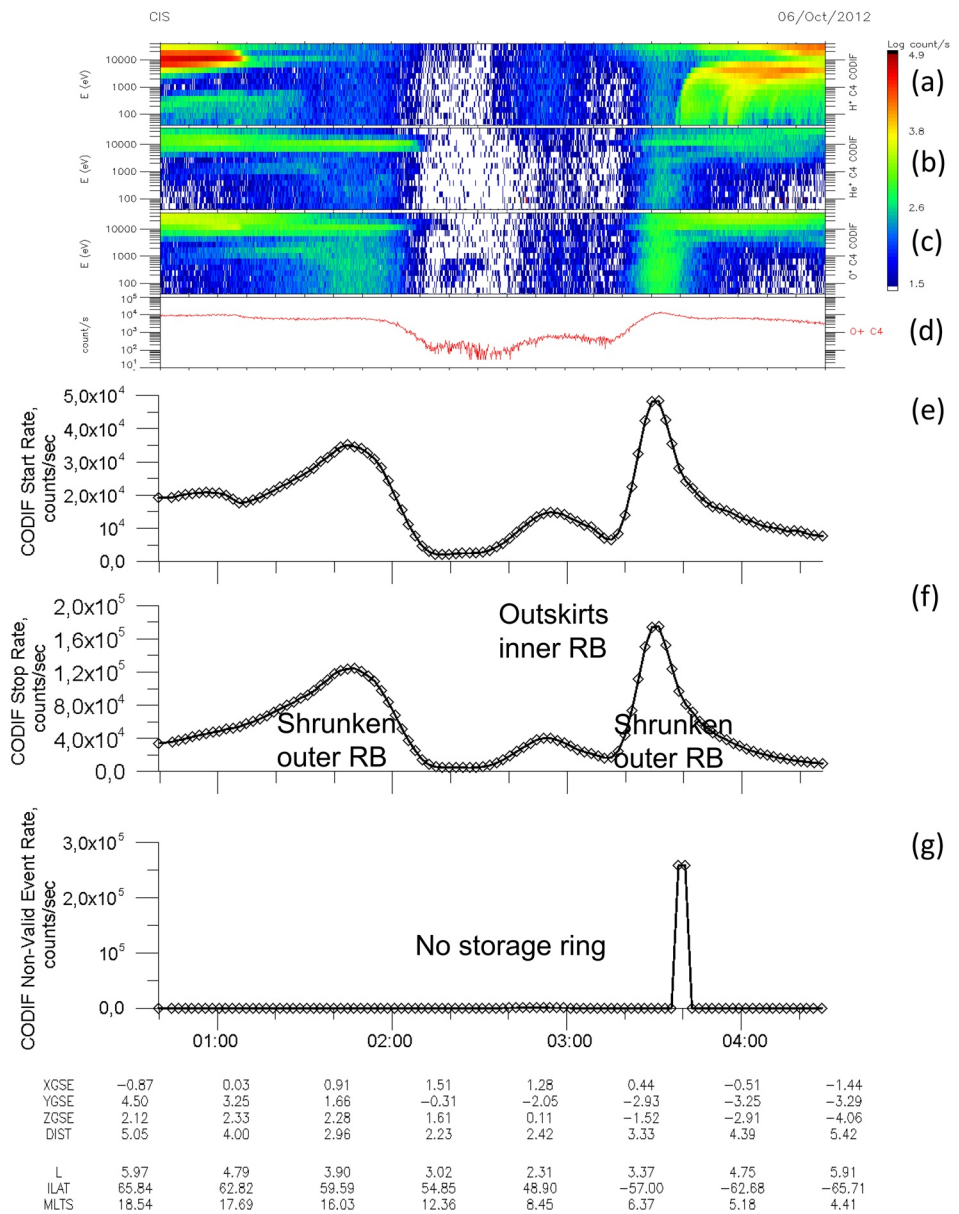


Figure 14. Absence of storage ring signatures as seen on Cluster CODIF data and in telemetry data (start, stop, and non-valid event rates) on October 6, 2012.

in the energy-time spectrograms. July–August 2007 and September–October 2012 time periods were used for method demonstration on a presence of a third radiation belt, or storage ring.

During July–August 2007 period, the signatures of the storage ring have persisted for almost a month clearly seen in Cluster HIA measurements. Among the previously analyzed data from April 2007 to June 2009, six periods were detected with clear presence of a storage ring (April 19–24, May 20, and November 19 in 2007 and May 23–30, June 1–13, and October 29 in 2008). The storage ring signatures can be easily seen in Cluster CIS spectrograms at <http://cluster.irap.omp.eu/public/spectro/>. During the September–October 2012 event, appearance, presence and disappearance of the storage ring observed by Cluster using the method of combination of CODIF O⁺ spectrograms and telemetry signals are in agreement with figures from Baker et al. (2013). As compared to the storage ring events determined from THEMIS data (Turner et al., 2013), out of 16 events provided by D. Turner and listed in Table 3 all had signatures also in Cluster data (when data were available), except for one on

Table 3

List of Storage Ring Events Obtained From THEMIS Data (Turner et al., 2013), Provided by D. Turner With Corresponding Events From Cluster

SR on THEMIS data	SR on Cluster data
26 March 2008	No data
02 May 2010	No data
03 August 2010	06 August 2010, 15–18 UT (HIA + CODIF)
04 February 2011	No data
01 March 2011	No data
27 May 2011	No data
17 September 2011	September 17 (12–18 UT) and 19 (18–24 UT), 2011 (HIA + CODIF)
24 October 2011	21 October 2011, 12–18 UT (HIA + CODIF)
24 January 2012	No data
09 March 2012	14 March 2012, 06–12 UT (CODIF)
04 April 2012	10 April 2012, 06–12 UT (CODIF)
12 April 2012	April 12 (12–18 UT) and 14 (18–24 UT), 2012 (CODIF)
23 April 2012	April 21, 2012, 12–18, 18–24 UT (CODIF)
01 September 2012	Shown in present paper
12 December 2012	No signatures
13 January 2013	09 January 2013, 00–06 UT (CODIF)

December 12, 2012. Starting from 2012, only CODIF data were used to determine the storage ring presence. Thus, this demonstrates that both methods, with and without HIA data, can serve as an additional source of information about radiation belts structure.

The obtained locations of the storage ring also provided its width. For the July–August 2007 period, the storage ring was situated at $3.0 < L < 4.2$ with its width ΔL between 0.1 and 0.9 as detected by Cluster and at $2.8 < L < 3.9$ and ΔL between 0.3 and 0.9 as seen by Double Star. For September–October 2012 event, the storage ring was located at $2.9 < L < 3.4$ with ΔL of 0.3–0.4. Baker et al. (2013) stated that the observed storage ring during that event stayed unchanged at $L \sim 3$ –3.5 for 4 weeks. Yuan and Zong (2013) gave the locations of the third radiation belt at $3 < L < 4$ with one event at $2 < L < 3$. Similar positions at L s between 3 and 4 were obtained by Turner et al. (2013), Kellerman et al. (2014), and Hao et al. (2020). Pinto et al. (2018) gave the range of L s between 2.8 and 3.8 for 30 identified three-belt events. L -shells and widths of the storage ring provided by our methods are in agreement with all previous studies. It is necessary to stress that the proposed methods are not meant to substitute particle measurements in the analysis of the radiation belts structure. The methods cannot be easily used in an automatic manner but requires some visual inspection. The detected background varies significantly depending on the satellite orbit, geomagnetic conditions, state of the instrument and so forth. In case of Cluster observations, telemetry raw data are also important. Telemetry raw data are not usually considered as a helpful addition and it requires more detailed knowledge of the satellite's characteristics. Nevertheless, the strength of these methods is the ability to provide a source of information on the radiation belts features when no other particle measurements are available at all but only background counts were detected.

Summarizing the results discussed above, the conclusions are the following:

1. Instrument background counts as seen in the case of the Cluster and Double Star satellites provide highly valuable information about the radiation belt features including temporary ones such as the storage ring.
2. As a new approach, telemetry raw counts on Cluster used when no HIA data were available and CODIF shielding restricts direct background analysis, register signals which increase due to penetrating particles even when no corresponding increases are shown in the CODIF energy-time spectrograms.
3. Applications of the background and telemetry combination approaches to the analysis of two periods when the storage ring was detected between the traditional outer and inner belts resulted in the agreement of the

obtained L-shells and widths of storage with those of the previous studies. The presented approaches are able to provide valuable information on the radiation belts features when no other particle measurements are available but only background counts.

Data Availability Statement

The data for solar wind, IMF data, and geomagnetic indices were obtained from OMNIWeb (<http://omniweb.gsfc.nasa.gov/>). The CIS and HIA data from both Cluster and Double Star are available at the Cluster Science Archive (CSA) (<https://csa.esac.esa.int/csa-web/>). CODIF telemetry data are all available at CSA (CIS ion spectrometer, Ancillary, Monitor Rates, product *CP_CIS – CODIF_HS_RATES*, parameter SF for CODIF Start Rate, SR for Stop Rate and NVE for Non-Valid Event Rate), processed by IFSIDL software which has been developed by Giuseppe Pallochia, of IAPS – INAF (Rome, Italy) and by clweb software (<http://clweb.irap.omp.eu/>) developed by Emmanuel Penou of IRAP.

Acknowledgments

The work of N. Ganushkina and M. Liemohn at the University of Michigan was partly supported by National Aeronautics and Space Administration grants NNX17AI48G, 80NSSC20K0353, NNX-17AB87G, and 80NSSC20K1504 grants. The contributions by N. Ganushkina were also partly supported by the Academy of Finland (grant 339329). French participation in the Cluster project has been supported in part by CNES (grant number to IRAP 4500065232).

References

- Baker, D. N., Jaynes, A. N., Kanekal, S. G., Foster, J. C., Erickson, P. J., Fennell, J. F., et al. (2016). Highly relativistic radiation belt electron acceleration, transport, and loss: Large solar storm events of March and June 2015. *Journal of Geophysical Research: Space Physics*, *121*(7), 6647–6660. <https://doi.org/10.1002/2016JA022502>
- Baker, D. N., Kanekal, S. G., Hoxie, V. C., Henderson, M. G., Li, X., Spence, H. E., et al. (2013). A long-lived relativistic electron storage ring embedded in earth's outer van Allen belt. *Science*, *340*(6129), 186–190. <https://doi.org/10.1126/science.1233518>
- Balogh, A., Carr, C. M., Acuña, M. H., Dunlop, M. W., Beek, T. J., Brown, P., et al. (2001). The cluster magnetic field investigation: Overview of in-flight performance and initial results. *Annales Geophysicae*, *19*(10/12), 1207–1217. <https://doi.org/10.5194/angeo-19-1207-2001>
- Carr, C., Brown, P., Zhang, T. L., Gloag, J., Horbury, T., Lucek, E., et al. (2005). The double star magnetic field investigation: Instrument design, performance and highlights of the first year's observations. *Annales Geophysicae*, *23*(8), 2713–2732. <https://doi.org/10.5194/angeo-23-2713-2005>
- Dandouras, I. (2013). Detection of a plasmaspheric wind in the earth's magnetosphere by the cluster spacecraft. *Annales Geophysicae*, *31*(7), 1143–1153. <https://doi.org/10.5194/angeo-31-1143-2013>
- Dandouras, I., Cao, J., & Vallat, C. (2009). Energetic ion dynamics of the inner magnetosphere revealed in coordinated cluster-double star observations. *Journal of Geophysical Research: Space Physics*, *114*(A1). <https://doi.org/10.1029/2007JA012757>
- Dandouras, I., Pierrard, V., Goldstein, J., Vallat, C., Parks, G. K., Réme, H., et al. (2005). Multipoint observations of ionic structures in the plasmasphere by cluster-cis and comparisons with image-EUV observations and with model simulations. In *Inner magnetosphere interactions: New perspectives from imaging* (p. 23–53). American Geophysical Union (AGU). <https://doi.org/10.1029/159GM03>
- Delory, G. T., Luhmann, J. G., Brain, D., Lillis, R. J., Mitchell, D. L., Mewaldt, R. A., & Falkenberg, T. V. (2012). Energetic particles detected by the electron reflectometer instrument on the mars global surveyor, 1999–2006. *Space Weather*, *10*(6). <https://doi.org/10.1029/2012SW000781>
- Escoubet, C. P., Fehringer, M., & Goldstein, M. (2001). Introduction to the cluster mission. *Annales Geophysicae*, *19*(10/12), 1197–1200. <https://doi.org/10.5194/angeo-19-1197-2001>
- Escoubet, C. P., Masson, A., Laakso, H., & Goldstein, M. L. (2015). Recent highlights from cluster, the first 3-d magnetospheric mission. *Annales Geophysicae*, *33*(10), 1221–1235. <https://doi.org/10.5194/angeo-33-1221-2015>
- Ganushkina, N. Y., Dandouras, I., Shprits, Y. Y., & Cao, J. (2011). Locations of boundaries of outer and inner radiation belts as observed by cluster and double star. *Journal of Geophysical Research: Space Physics*, *116*(A9). <https://doi.org/10.1029/2010JA016376>
- Hao, Y. X., Zong, Q.-G., Zhou, X.-Z., Zou, H., Rankin, R., Sun, Y. X., et al. (2020). A short-lived three-belt structure for sub-mev electrons in the van Allen belts: Time scale and energy dependence. *Journal of Geophysical Research: Space Physics*, *125*(9), e2020JA028031. <https://doi.org/10.1029/2020JA028031>
- Kasahara, S., Asamura, K., Ogasawara, K., Kazama, Y., Takashima, T., Hirahara, M., & Saito, Y. (2009). A noise attenuation method for medium-energy electron measurements in the radiation belt. *Advances in Space Research*, *43*(5), 792–801. <https://doi.org/10.1016/j.asr.2008.11.012>
- Kellerman, A. C., Shprits, Y. Y., Kondrashov, D., Subbotin, D., Makarevich, R. A., Donovan, E., & Nagai, T. (2014). Three-dimensional data assimilation and reanalysis of radiation belt electrons: Observations of a four-zone structure using five spacecraft and the verb code. *Journal of Geophysical Research: Space Physics*, *119*(11), 8764–8783. <https://doi.org/10.1002/2014JA020171>
- Kistler, L. M., Moukis, C. G., & Genestreti, K. J. (2013). In-flight calibration of the cluster/CODIF sensor. *Geoscientific Instrumentation, Methods and Data Systems*, *2*(2), 225–235. <https://doi.org/10.5194/gi-2-225-2013>
- Liu, Z. X., Escoubet, C. P., Pu, Z., Laakso, H., Shi, J. K., Shen, C., & Hapgood, M. (2005). The double star mission. *Annales Geophysicae*, *23*(8), 2707–2712. <https://doi.org/10.5194/angeo-23-2707-2005>
- Mann, I. R., Lee, E. A., Claudepierre, S. G., Fennell, J. F., Degeling, A., Rae, I. J., et al. (2013). Discovery of the action of a geophysical synchrotron in the Earth's van Allen radiation belts. *Nature Communications*, *4*, 2795. <https://doi.org/10.1038/ncomms3795>
- Pinto, V. A., Bortnik, J., Moya, P. S., Lyons, L. R., Sibeck, D. G., Kanekal, S. G., et al. (2018). Characteristics, occurrence, and decay rates of remnant belts associated with three-belt events in the earth's radiation belts. *Geophysical Research Letters*, *45*(22), 12099–12107. <https://doi.org/10.1029/2018GL080274>
- Pinto, V. A., Mourenas, D., Bortnik, J., Zhang, X.-J., Artemyev, A. V., Moya, P. S., & Lyons, L. R. (2019). Decay of ultrarelativistic remnant belt electrons through scattering by plasmaspheric HISS. *Journal of Geophysical Research: Space Physics*, *124*(7), 5222–5233. <https://doi.org/10.1029/2019JA026509>
- Rème, H., Aoustin, C., Bosqued, J. M., Dandouras, I., Lavraud, B., Sauvaud, J. A., et al. (2001). First multispacecraft ion measurements in and near the earth's magnetosphere with the identical cluster ion spectrometry (cis) experiment. *Annales Geophysicae*, *19*(10/12), 1303–1354. <https://doi.org/10.5194/angeo-19-1303-2001>
- Rème, H., Dandouras, I., Aoustin, C., Bosqued, J. M., Sauvaud, J. A., Vallat, C., et al. (2005). The HIA instrument on board the TAN CE 1 double star near-equatorial spacecraft and its first results. *Annales Geophysicae*, *23*(8), 2757–2774. <https://doi.org/10.5194/angeo-23-2757-2005>

- Shprits, Y. Y., Horne, R. B., Kellerman, A. C., & Drozdov, A. Y. (2018). The dynamics of van Allen belts revisited. *Nature Physics*, *14*, 102–103. <https://doi.org/10.1038/nphys4350>
- Shprits, Y. Y., Subbotin, D., Drozdov, A. Y., Usanova, M. E., Kellerman, A. C., Orlova, K., et al. (2013). Unusual stable trapping of the ultrarelativistic electrons in the van Allen radiation belts. *Nature Physics*, *9*, 699–703. <https://doi.org/10.1038/nphys2760>
- Turner, D. L., Angelopoulos, V., Li, W., Hartinger, M. D., Usanova, M., Mann, I. R., et al. (2013). On the storm-time evolution of relativistic electron phase space density in earth's outer radiation belt. *Journal of Geophysical Research: Space Physics*, *118*(5), 2196–2212. <https://doi.org/10.1002/jgra.50151>
- Yuan, C., & Zong, Q. (2013). The double-belt outer radiation belt during CME- and CIR-driven geomagnetic storms. *Journal of Geophysical Research: Space Physics*, *118*(10), 6291–6301. <https://doi.org/10.1002/jgra.50564>